POLYPUBLIE
Polytechnique Montréal

POLYTECHNIQUE MONTRÉAL
UNIVERSITÉ D'INGÉNIERIE

Titre: Title:	Real-time electromagnetic signal processing: principles and illustrations
Auteurs: Authors:	Shulabh Gupta, & Christophe Caloz
Date:	2017
Type:	Chapitre de livre / Book Section
Référence: Citation:	Gupta, S., & Caloz, C. (2017). Real-time electromagnetic signal processing: principles and illustrations. Dans Costanzo, S. (édit.), Wave Propagation Concepts for Near-Future Telecommunication Systems (155-176). https://doi.org/10.5772/67356

Document en libre accès dans PolyPublie
Open Access document in PolyPublie

URL de PolyPublie: PolyPublie URL:	https://publications.polymtl.ca/4717/
Version:	
Conditions d'utilisation: Terms of Use:	CC BY

Document publié chez l'éditeur officiel
Document issued by the official publisher

Titre du livre: Book Title:	Wave Propagation Concepts for Near-Future Telecommunication Systems
Maison d'édition: Publisher:	IntechOpen
URL officiel: Official URL:	https://doi.org/10.5772/67356
Mention légale: Legal notice:	

We are IntechOpen,
the world's leading publisher of
Open Access books
Built by scientists, for scientists

5,400
Open access books available

134,000
International authors and editors

165M
Downloads

Our authors are among the

154
Countries delivered to

TOP 1%
most cited scientists

12.2%
Contributors from top 500 universities

BOOK CITATION INDEX
CLARIVATE ANALYTICS
INDEXED

WEB OF SCIENCE™

Selection of our books indexed in the Book Citation Index
in Web of Science™ Core Collection (BKCI)

Interested in publishing with us?
Contact book.department@intechopen.com

Real-Time Electromagnetic Signal Processing: Principles and Illustrations

Shulabh Gupta and Christophe Caloz

Additional information is available at the end of the chapter

http://dx.doi.org/10.5772/67356

Abstract

Real-time electromagnetic signal processing has recently appeared as a novel signal-processing paradigm to manipulate and control electromagnetic signals in real time directly in the analog domain. This has led to attractive alternatives to conventional digital techniques, which typically suffer from poor performances and high cost at microwave and millimeter wave frequencies. This novel paradigm is based on dispersion-engineered electromagnetic structures, and in this review chapter, two types of structures are presented and discussed in details: phasers and metasurfaces. While phasers are typically group delay engineered to manipulate and rearrange spectral components in the time domain, metasurfaces enhances these functionalities by providing spatial processing in addition to temporal processing. Two kinds of phasers are presented here: static and dynamic all-pass C-section phasers, and all-dielectric metasurface-based spatial phasers. Finally, two applications illustrating real-time signal processing are discussed: 2D beam scanning leaky-wave antenna for high-resolution spectrum analysis and a dispersion code multiple access (DCMA) system.

Keywords: analog signal processing, dispersion engineering, real-time systems, metamaterials, metasurfaces, all-pass systems, phasers, leaky-wave antennas, spectrum analyzers, dispersion modulation systems

1. Introduction

Recent decade developments in wireless communications may be described in terms of the evolution of the fundamental nature of corresponding services, which are referred to as mobile generations, not compatible with the previous cellular standards. The first mobile generation (1G) was based on analog transmission. Its evolution in 1992 into the second mobile generation (2G), introducing digital transmission, represented a major technological advance. The third

mobile generation (3G) appeared in 2001 and brought multimedia support, spread spectrum access, and peak bit rate exceeding 200 kbit/s. Since 2011/2012, the prevailing technology has been the fourth mobile generation (4G), which covers Internet protocol (IP) packet-switched networks and thus provides ultrabroadband (Gbit/s speed) mobile access. 4G systems use the LTE (Long Term Evolution) standard, which embodies an OFDMA (Orthogonal Frequency Division Multiple Access) scheme for base station and a hybrid SCOFDM (Single Carrier OFDM) for multiple access. Thus, each mobile generation has evolved into a new generation about every 10 years to keep up with the ever-rising demands by end-consumers. The fifth mobile generation (5G) standards are expected to be established around 2019/2020 and 5G networks should be deployed between 2020 and 2030 [1, 2].

Extrapolating from current market trends of rising consumer demand and financial growth in the mobile technology, it is predicted that 5G networks will be required to support a 1000-fold increase in data capacity to handle over 100 billion devices featuring peak rates of 10 Gb/s and low data transmission latency [3]. The bandwidth of current microwave cellular systems is around 600 MHz, and it is divided among different communication operators. While efforts have been made to increase the operation bandwidth for higher data throughput, the best attempts have led to an increase of only 80 MHz. Moreover, this increase comes at a high cost in terms of modification requirements of existing infrastructures. Due to these issues, some amendments have been operated in current IEEE 802.11 networks, in particular, advancement toward 5G with the introduction of IEEE 802.11ad for exploiting the 60 GHz millimeter-wave spectrum. However, current 802.11ad is still based on single carrier OFDM and is limited in terms of the achievable peak data rate. Therefore, it clearly appears that a mere evolution of current mobile technologies will be largely insufficient to meet the anticipated demands of 5G networks. There is a most pressing need for disruptive technological solutions [4, 5].

In order to address the aforementioned challenges of 5G networks, two potential disruptive directions have been suggested, both related to the physical layers [4]: (1) transition to millimeter-wave frequency bands to leverage their huge available spectrum and hence achieve drastic channel capacity enhancement and (2) deployment of massive MIMO systems with advanced beam-forming techniques providing various cognitive features, such as for instance smart channel detection. While millimeter-wave frequencies transition aims at wider spectrum usage, cognition and multiple access techniques are targeted for more efficient spectral efficiency [4]. Smart cognitive functions involve the automated identification of free channels in mobiles and base stations for better exploitation of the channels' potential. For instance, beam-division multiple access (BDMA) maximizes the spectrum efficiency by dividing antenna beams according to the available angular sectors of mobile stations. BDMA offers an attractive multiple access approach but suffers from excessive high-speed signal processing requirements, and hence with potentially prohibitive cost and complexity for 5G [6].

Realizing the considerable potential of millimeter-wave technologies, the WiFi alliance recently introduced the WiGig standard (802.11ad), which targets several applications in the 60 GHz range [7]. Among these applications is small-cell mobile backhaul, which consists of fixed interconnections of mobile service base stations to the backbone network. WiGig backhaul will enhance mobile speed access by using point-to-point microwave and millimeter-wave radio

links [8]. Another application, already in use currently, is that of data center interconnects, where point-to-point wireless links replace cumbersome cables and introduce real-time network configurability [8, 9]. These interconnects have been shown to exhibit superior cost and atmospheric loss performance [4] than free-space optics (FSO) systems [10]. While IEEE 802.11ad uses the licensed band around 60 GHz, other frequency bands with comparable signal propagation characteristics through the atmosphere are available, in particular, the 71–76, 81–86, and 92–95 GHz bands. Overall, millimeter-wave frequency operation enables directive transmission, reduced signal interference, and enhanced signal-to-noise ratio in a wide spectrum range [11].

While transition to millimeter-wave may simplify system architectures, it also requires major technological progress in terms of hardware constraints. Current systems heavily rely on digital techniques, whose high-power consuming mixed signal subsystems, which require ultrafast analog-to-digital (ADC) and digital-to-analog converters (DAC), become prohibitive in such high-frequency and large-bandwidth regimes [4]. In particular, conventional microwave architectures, where each antenna is connected to an ADC/DAC, are inapplicable to millimeter-wave systems unless a spectacular technological breakthrough occurs in electronics technology. As of today, millimeter-wave systems must resort to hybrid architectures, where a significant part of the signal processing is performed at baseband, implying high system complexity and cost. More importantly, this approach is highly restricted in operation bandwidth, which defeats the original purpose of accessing wider spectrum resources at millimeter-waves.

Considering the exploding demand increase of 5G in data capacity and the inability of current technology to meet the related challenges, a paradigm-shifting breakthrough is clearly needed for millimeter-wave communication systems. While the conventional wisdom points toward baseband and RF architectures, with the aim of realizing computationally efficient interfaces and higher density integrated designs, this chapter presents a fundamentally different and a potentially disruptive signal processing technology, which does not depend on digital techniques and hence without suffering from their technological bottlenecks. This signal processing paradigm is called radio-analog signal processing or R-ASP in short.

2. Radio analog signal processing (R-ASP)

R-ASP might be defined as the manipulation of signals in their pristine analog form and in real time to realize specific operations enabling microwave or mm-wave and terahertz applications [12]. The concept of R-ASP can be best understood by considering the two basic effects illustrated in **Figure 1**, chirping with time spreading and frequency discrimination in the time domain. Both effects involve a linear device with transfer function $H(\omega) = e^{j\varphi(\omega)}$, assumed to be of unity transmission magnitude and whose phase, $\varphi(\omega)$, is a nonlinear frequency function, or whose group delay, $\tau(\omega) = \partial\varphi(\omega)/\partial\omega$, is a function of frequency. Such an element, with *frequency-dependent group delay*, is called *temporally dispersive*. The bandwidth of $H(\omega)$ is assumed to cover the entire spectrum of the input signal.
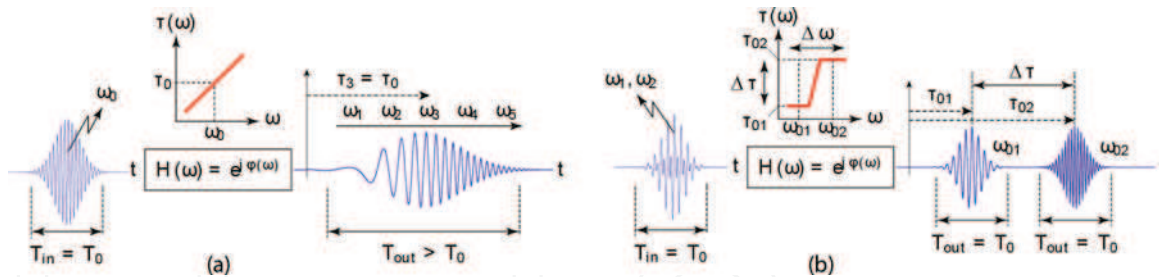
Figure 1. Basic effects in R-ASP. (a) Chirping with time spreading and (b) frequency discrimination in the time domain. ©IEEE; reprinted with permission.

In the first case, shown in **Figure 1(a)**, a pulse modulated at a frequency ω_0 is injected into a dispersive element, which exhibits a positive linear group delay slope over a frequency band centered at the ω_0, corresponding to a group delay τ_0. Due to the dispersion of this element, the different frequency components of the pulse experience different phase-shifts and therefore appear at different times. Here, the lower-frequency components are delayed less than the higher-frequency components and therefore appear earlier, while the center-frequency component appears at the time $\tau_3 = \tau_0$. This results in an output pulse whose instantaneous frequency is progressively increasing, a phenomenon called "chirping," and which has experienced time spreading ($T_{out} > T_0$), accompanied with reduced amplitude due to energy conservation.

In the second case, depicted in **Figure 1(b)**, the input pulse is modulated by a two-tone signal, with frequencies ω_{01} and ω_{02}, and passed through a dispersive element $H(\omega)$ exhibiting a positive stepped group delay, with two steps, centered at ω_{01} and ω_{02}, respectively. Based on this dispersive characteristic, the part of the pulse modulated at the lower frequency, ω_{01}, is delayed less than the part modulated at the higher frequency, ω_{02}, and hence emerges earlier in time. As a result, the two pulses are *resolved* (or separated) in the time domain, and their respective modulation frequencies may be deduced from their respective group delays from the dispersive transfer function, $H(\omega)$. Note that with the flat-step group delay considered here the pulses are *not* time-spread ($T_{out} = T_0$), assuming that the pulse bandwidth fits in the flat bands of the steps.

The R-ASP technology is widely applicable in areas such as instrumentation, sensing, security, all-analog communication systems, and dynamic and cooperative data wireless networks. Consequently, R-ASP has already led to wealth of novel applications such as real-time Fourier transformers [13], spectrum sniffers, discriminators and frequency meters [14–16], radio-frequency identification (RFID) systems [17], spatial spectrum analyzers [18, 19], pulse-position modulators (PPM) [20], DCMA system [21], dispersion code modulation [22], signal-to-noise ratio enhancer [23], frequency-division-modulators (FDM) [24], etc.

3. Electromagnetic phasers

The heart of an R-ASP system is a phaser, which is a component exhibiting a specified frequency-dependent group-delay response within a given frequency range, as described above [12].

Phasers are either reflection type or transmission type. Reflection-type phasers are single-port structures, which are transformed into two-port structures using a broadband circulator or a hybrid coupler. They are mostly based on Bragg reflections and include microstrip-chirped delay lines [25] and reflection-type waveguide phasers [26]. While reflection-type phasers suffers from less constraints in the design parameters compared to transmission-type phasers, their requirement of an external one-port to two-port conversion component, resulting in additional loss along with undesired phase distortions, is a major drawback. Transmission-type phasers, on the other hand, are inherently two-port components. Surface acoustic wave (SAW) devices [27], and magnetostatic devices [28] are good for designing high dispersion phasers; however, they are suitable only for very low frequencies and narrow-bandwidth applications. While some recently proposed transmission-type phasers, based on coupled-matrix analysis, features great design flexibility for advanced group delay engineering, they are typically restricted to narrow-band designs [29, 30]. For broader-band applications, coupled-line all-pass phasers are more suitable, offering also greater design simplicity and benefiting from efficient synthesis procedures [31, 32].

The coupled-line all-pass phasers reported to date are based on cascaded C-sections (CCS) and/or D-sections synthesizing prescribed group delay responses [33]. On the other hand, a longitudinal cascade of commensurate coupled transmission-lines, or cascaded coupled-line (CCL) phaser, was first demonstrated in Ref. [31]. A hybrid configuration based on the combination of a CCS and a CCL configuration, known as hybrid cascade (HC) coupled-line phaser was recently proposed in Ref. [34]. This set of three cascading configurations, CCL, CCS, and HC, represent the fundamental cascading schemes upon which more complex phasers can be constructed, leading to vast variety of coupled-line all-pass phasers with rich and exotic dispersion characteristics.

3.1. Passive coupled-line all-pass phasers

3.1.1. Basic transfer functions

Transmission all-pass transfer functions are constructed using two building-block transfer functions: the C-section and the D-section transfer functions [31]. A C-section transfer function can be realized by a two-port transmission-line device, consisting of a contra-directional coupled-line coupler, whose through and isolated ports are interconnected by an ideal transmission-line section, as shown in **Figure 2(a)**. Its transfer function can be obtained by applying the connecting boundary condition between the ingoing and outgoing waves at the two isolated and coupled ports of the coupler. The C-section transfer function is given by:

$$S_{21}(\theta) = \left(\frac{\rho - j\tan\theta}{\rho + j\tan\theta} \right), \quad \text{with} \quad \rho = \sqrt{\frac{1+k}{1-k}} \tag{1}$$

where k is the coupling coefficient between the coupled lines forming the structure. Its all-pass nature, $|S21| = 1$, $\forall\theta$, can be verified by observing that the magnitudes of the numerator and denominator in Eq. (1) are equal, and that the function provides a frequency-dependent group delay response with a maxima at $\theta = (2m - 1)\pi/2$, where m is an integer. This condition corresponds to frequencies where the length of the coupled-line section is an odd multiple of

a quarter wavelength. Upon the high-pass to low-pass transformation $s = j \tan \theta$, the C-section is seen to be a first-order phaser, with one real pole and one real zero, placed symmetrically about the imaginary axis in the s-plane.
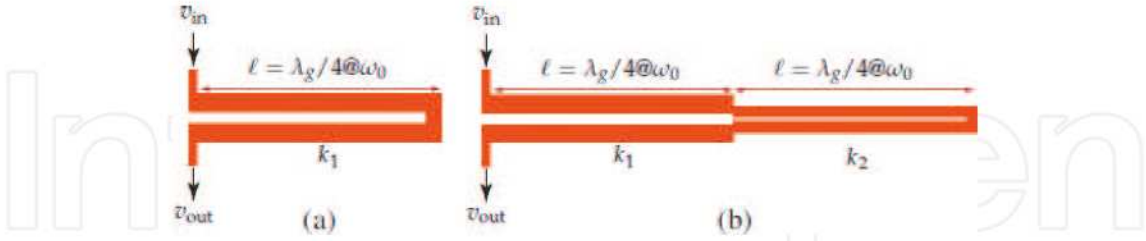

Figure 2. Transmission-type all-pass phaser topologies. (a) C-section and (b) D-section, with ω_0 being the quarter-wavelength frequency of a transmission line [34]. ©IEEE; reprinted with permission.

The derivation of a generalized transfer function corresponding to a coupled-line coupler terminated with an arbitrary all-pass load with transfer function $S0$ is provided in reference [34], and reads

$$S_{21}(\theta) = b + \frac{a^2 S_0}{1 - bS_0} \tag{2}$$

where in Eq. (2) a and b are the through and coupled transfer functions of the isolated coupler. The C-section transfer function is a particular case of this network with $S_0 = 1$.

The second-order all-pass phaser is the D-section, which consists of a contra-directional coupled-line coupler terminated with a C-section, as shown in **Figure 2(b)**. Using the transfer function from Eq. (2) with S_0 corresponding to a C-section, i.e., Eq. (1), the transfer function of a D-section is found as

$$S_{21}(\theta) = \left(\frac{1 - \rho_a \tan\theta^2 - j\rho_b \tan\theta}{1 - \rho_a \tan\theta^2 + j\rho_b \tan\theta} \right), \rho_a = \sqrt{\frac{1-k_1}{1+k_2}}\sqrt{\frac{1+k_1}{1-k_2}}, \rho_b = \sqrt{\frac{1-k_1}{1+k_1}}\sqrt{\frac{1-k_1}{1+k_2}}, \tag{3}$$

where $k_{1,2}$ are the coupling coefficients of the two sections. Upon the transformation $s = j \tan \theta$, the D-section is seen to be a second-order phaser, with two pairs of complex para-conjugate zeros and poles in the s-plane.

3.1.2. Phaser topologies

The C-section and a D-section group delay profiles have a specific and restricted shape that depends on the specific length and coupling coefficients of the sections. However, exploiting several coupled-line sections in a flexible fashion allows synthesizing virtually arbitrary pre-scribed group delay responses between the input and the output ports for a given bandwidth. Such phasers can be categorized based on how the different coupled-line sections are connected together. The three possible basic configurations shown in **Figure 3** are next described.
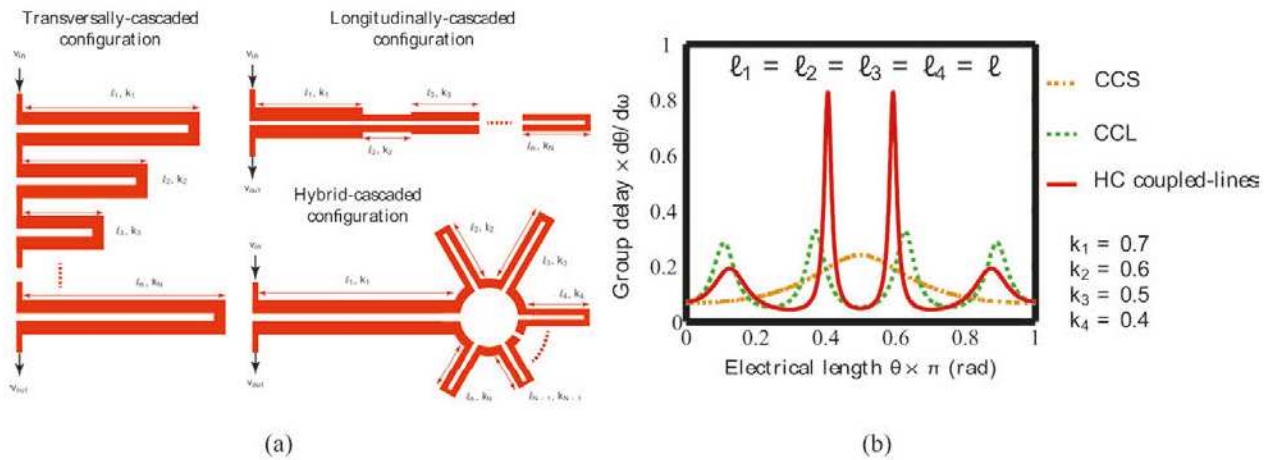
Figure 3. Cascaded coupled-line all-pass phasers [34]. (a) Generic topologies for a cascaded C-sections (CCS), cascaded coupled-lines (CCL) and hybrid-cascaded (HC) coupled-line phasers. (b) Typical group delay response of the three phaser topologies in (a) over the lowest coupled-line section harmonic frequency band with $N = 4$ coupled-line sections of identical length $l_i = 1$. ©IEEE; reprinted with permission.

1. *Cascaded C-section (CCS) phaser.* When several C-sections are cascaded in the direction that is transverse to the axis of the transmission lines forming the C-sections, as shown in **Figure 3(a)**, a CCS configuration is formed. The resulting transfer function is then simply the product of the individual C-section transfer functions and is given by

$$S_{21}^{CCS}(\theta) = \prod_{i=2}^{N} \frac{\rho_i - j\tan\theta}{\rho_i + j\tan\theta}, \tag{4}$$

where $\rho_i = (1 + k_i)/(1 - k_i)$, k_i being the coupling coefficient of the ith section.

2. *Cascaded coupled-lines (CCL) phaser.* In this configuration, several coupled-line sections are cascaded in the direction of the transmission lines forming the coupled-lines, as shown in **Figure 3(a)**, with the last section being a C-section Cristal [31]. The corresponding transfer function can be derived by iteratively constructing the load transfer functions starting from the last coupled-line section toward the input port, as derived by Gupta et al. [34]. The result is

$$S_{21}^{CCL}(\theta) = b_1 + \frac{a_1^2 S_2(\theta)}{1 - b_1 S_2(\theta)}, \tag{5}$$

where $S_2(\theta)$ is the overall transfer function of the structure starting from the 2nd to the Nth coupled-line section. It is to be noted that a D-section is the particular case of a CCL coupled-line phaser with $N = 2$.

3. *Hybrid-cascaded (HC) coupled-line phaser.* This configuration is based on a combination of CCS and CCL sections, as illustrated in **Figure 3(c)**. This configuration can be seen as a coupled-line coupler terminated with a CCS phaser. The corresponding transfer function can be derived by substituting the CCS transfer function as S_0 in Eq. (2), resulting in

$$S_{21}^{HC}(\theta) = b_1 + \frac{a_1^2 S_0(\theta)}{1 - b_1 S_0(\theta)}, \quad S_0(\theta) = \prod_{i=2}^{N} \dot{\frac{\rho_i - j\tan\theta}{\rho_i + j\tan\theta}}, \tag{6}$$

The diversity of possible delay functions provided by the CCS, CCL, and HC coupled-line phasers is too great to be tractable in such a chapter. Therefore, for the sake of simplicity, we shall restrict our analysis to the case of commensurate coupled-line sections having all the same lengths. However, it should be kept in mind that the above transfer functions are general and that the phasers exhibit much richer synthesis possibilities than those presented next.

3.1.3. Group delay response

The three configurations in **Figure 3(a)** exhibit very different group delay responses, as shown in **Figure 3(b)** for the case of $N = 4$ and $l_1 = l_2 = l_3 = l_4 = l$. For the second condition, the CCS phaser has a delay shape similar to that of a regular C-section, with a single delay maximum in $\theta \in [0, \pi]$. In contrast, the CCL configuration exhibits four delay peaks. These peaks are quasi-uniformly spaced and quasi-equal in magnitude, with group delay swings, $\Delta\tau = \tau_{max} - \tau_{min}$, that are larger than those obtained in the CCS case. Similar to the CCL case, the HC coupled-line phaser exhibits four delay peaks, but with significantly different characteristics. While the outermost delay peaks are lower, the middle ones have a steep slope within a narrow bandwidth and thus exhibit a very large delay swing $\Delta\tau$. Thus, for a given maximum achievable coupling k, for the three configurations, the HC coupled-line phaser provides the largest group delay swing $\Delta\tau$.

3.2. Active and reconfigurable C-section all-pass phasers

The above phasers are fixed in group delay profiles. However, there are some occasions requiring reconfigurability in group delay response when the radio systems need to be adaptive in a dynamic environment. One example is the recently proposed DCMA system [21], where the communication between any two users requires the real-time establishment of a pair of complementary dispersion codes at the transmitter and receiver ends, respectively. In a time-variant environment, dynamically increasing the group delay swing may mitigate the interference and hence improve the signal-to-noise ratio.

To address such requirements, the group delay and amplitude response of a C-section phaser can be tuned by varying the amplitude of the transfer function of the loading network S_0. This leads to a reconfigurable all-pass phaser, where all-pass amplitude is obtained by cascading a pair of gain and loss loaded C-sections [35, 36].

3.2.1. Single loaded C-section

Figure 4(a) shows a single loaded C-section, consisting of a coupled-line coupler and a loading network connected at one end of the coupler.
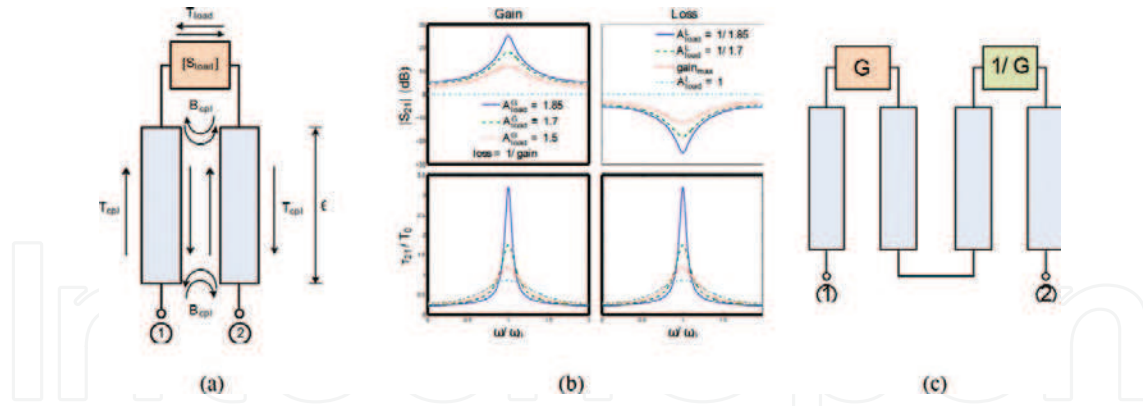
Figure 4. Proposed active reconfigurable all-pass phaser by cascading a gain-loss pair. (a) Loaded C-section [35] and (b) amplitude |S21| and normalized group delay τ/T_0 of the gain/loss loaded C-section, where the coupling factor $k = 0.5$ at ω_0. (c) Loss-gain all-pass C-section pair. ©IEEE; reprinted with permission.

The loading network, assuming perfect matching, is represented by the two-port S-parameters,

$$S_{\text{load}_{2 \times 2}} = \begin{bmatrix} 0 & T_{\text{load}} \\ T_{\text{load}} & 0 \end{bmatrix}, \text{ with } T_{\text{load}} = A_{\text{load}}(\omega)e^{j\varphi_{\text{load}}(\omega)}, \text{ with} \tag{7}$$

For simplicity, let $\varphi_{\text{load}}(\omega) = 0$ and $A_{\text{load}}(\omega) = A_{\text{load}}$, where A_{load} is a real constant. The coupled-line coupler is characterized by the four-port S-parameters

$$S_{cpl_{4 \times 4}} = \begin{bmatrix} 0 & T_{cpl} & 0 & B_{cpl} \\ T_{cpl} & 0 & B_{cpl} & 0 \\ 0 & B_{cpl} & 0 & T_{cpl} \\ Bs_{cpl} & 0 & T_{cpl} & 0 \end{bmatrix}, \text{ where} \tag{8a}$$

$$B_{cpl}(\omega) = \frac{jk \sin\theta}{\sqrt{1-k^2}\cos\theta + j\sin\theta}, \quad T_{cpl}(\omega) = \frac{\sqrt{1-k^2}}{\sqrt{1-k^2}\cos\theta + j\sin\theta}, \tag{8b}$$

are the backward coupling and through responses respectively, with the parameters, k and $\theta = \pi\omega/2\omega_0$, being the nominal coupling factor at the center frequency ω_0 and the electrical length of the coupler, respectively.

Connecting the loading network and the coupler as shown in **Figure 4(a)** yields the two-port S-parameters of the loaded C-section, which read: $S_{11}(\omega) = S_{22}(\omega) = 0$,

$$S_{21}(\omega, A_{\text{load}} = G) = G \cdot \frac{\sqrt{1-k^2}\cot\theta + j(1+k/G)}{\sqrt{1-k^2}\cot\theta + j(1+kG)} \tag{9}$$

3.2.2. Parametric study and all-pass paired gain-loss C-section unit

We can easily verify that Eq. (9) exhibits the following properties:

$$S_{21}(\omega, G) = \frac{1}{S_{21}\left(\omega, \frac{1}{G}\right)}, \text{ and } \tau_{21}(\omega, G) = \frac{1}{\tau_{21}\left(\omega, \frac{1}{G}\right)} \tag{10}$$

respectively, with $G > 1$ as gain. Eq. (10) states that two loaded C-sections with opposite amplitudes, G and $1/G$, exhibit identical group delay responses and reciprocal amplitude responses. **Figure 4(c)** shows the responses, Eq. (**10**), with fixed coupling factor $k = 0.5$ and varying gain and loss, G and $1/G$, of the loading networks.

Therefore, cascading the paired gain and loss loaded C-sections leads to an all-pass C-section unit, as shown in **Figure 4(b)**. The amplitude and group delay responses of the resulting all-pass paired gain-loss C-section unit are respectively.

$$|S_{21}^{AP}(\omega)| = |S_{21}(\omega, G)| \bullet |S_{21}\left(\omega, \frac{1}{G}\right)| = 1 \tag{11}$$

$$\tau_{21}^{AP}(\omega) = \tau_{21}(\omega, G) + \tau_{21}(\omega, G) = 2\tau_{21}(\omega, G), \tag{12}$$

3.2.3. Reconfigurable phaser using gain-loss C-sections and numerical demonstration

We can now cascade N gain-loss C-section units, as shown in **Figure 5**, to synthesize arbitrary group delay responses. The ith constituent unit is tuned at center frequency $\omega_{0i} = 2\pi f_{0i}$ and assigned to the loading networks a gain-loss pair, G_i and $1/G_i$, respectively. The coupling factor, denoted as k, is the same for all units.

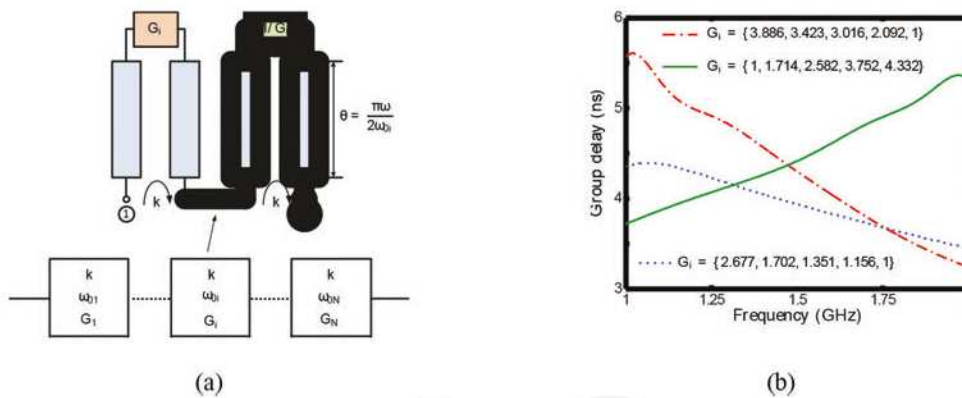(a)   (b)

Figure 5. *N*-unit all-pass reconfigurable phaser based on the paired gain-loss C-section unit shown in **Figure 4(c)** [35]. ©IEEE; reprinted with permission.

An $N = 5$ unit numerical example, where $k = 0.2$ and center frequency $f_{0i} = \{1, 1.25, 1.5, 1.75, 2\}$ GHz, is given. **Figure 5** shows three different group delay profiles along with the corresponding three different sets of controlling gain. Enhancement of the group delay swing and the reversed slope of the group delay curve is achieved [35, 36].

3.3. Spatial phasers

Phasers so far considered are all guided-wave in nature such as the ones based on coupled-line couplers as recalled in **Figure 6(a)**. The phaser converts an input pulse, $v_{in}(t)$, according to its specified group delay profile, $\tau(\omega)$, into a dispersed signal, $v_{out}(t)$. The same operation can also

be performed in the space-domain using a spatial component with an incident pulsed wave-front, $v_{in}(x,y,t)$, as shown in **Figure 6(b)**. Such a device is called a *spatial phaser*. For the sake of simplicity, the input wave is assumed to be a plane-wave polarized along the x-axis. The ideal response of a spatial phaser is an all-pass response, i.e., $|T_{xx}(\omega)| = 1$, with a specified dispersion $\tau_{xx} = \tau_{xx}(\omega) = \cdot\, d\{\angle T_{xx}(\omega)\}/d\omega$. Such a spatial phaser can also be realized using metasurfaces.
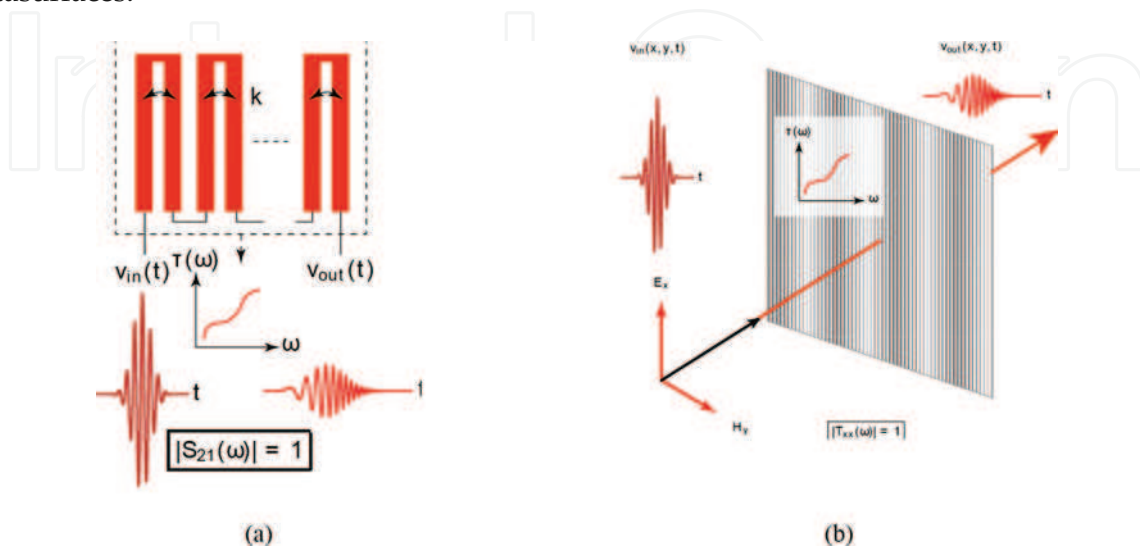

Figure 6. Phasers [12]. (a) Conventional guided-wave phasers and (b) proposed spatial phasers. ©IEEE; reprinted with permission.

A conventional phaser, shown in **Figure 6(a)**, is typically a series connection of C or D sections used in the hybrid configuration of **Figure 3** [34]. For example, a microwave C-section is a dispersive basic building block, where cascading C-sections of different frequency and delay characteristics, provides a specified group delay response. In a similar way, a spatial phaser, represented in **Figure 6(b)**, can be implemented by spatially cascading of all-pass spatial building blocks featuring different transmission delay characteristics [37]. These spatial all-pass units will be described next.

3.3.1. Conventional all-dielectric metasurface

Metasurfaces are spatial arrays made of subwavelengthly spaced scattering particles providing unprecedented flexibility in controlling electromagnetic wavefronts in space, time, or both space and time [38–42]. Recently, there has been a great interest in all-dielectric metasurfaces due to their low-loss characteristics and fabrication simplicity, as compared to their plasmonic implementations. All-dielectric metasurface structures are commonly based on coupled dielectric resonator unit cells, which simultaneously provide broadband full-transmission and 2π phase coverage, as a result of constructive interference between their electric and magnetic dipole responses [43, 44].

Figure 7(a) shows a conventional all-dielectric metasurface structure, consisting of a 2D array of coupled dielectric resonators of permittivity ε_r: (1) in a host dielectric layer of permittivity ε_r and (2) when a plane wave, $v_{in}(x,y,t)$ is incident on the unit cell, the electric and magnetic

dipole responses of the dielectric resonators are excited. If the resonators are designed such that the induced electric dipoles p and magnetic dipoles m are excited at the same frequency and have the same quality factor, then zero backscattering and thereby full transmission in the forward direction is achieved. While the host dielectric is not a fundamental component of the metasurface, it is just needed to provide mechanical support to the resonator array. Due the corresponding dielectric layered structure, spurious Fabry-Perot resonances may appear within the host substrate, contaminating the desired transmission response [43].
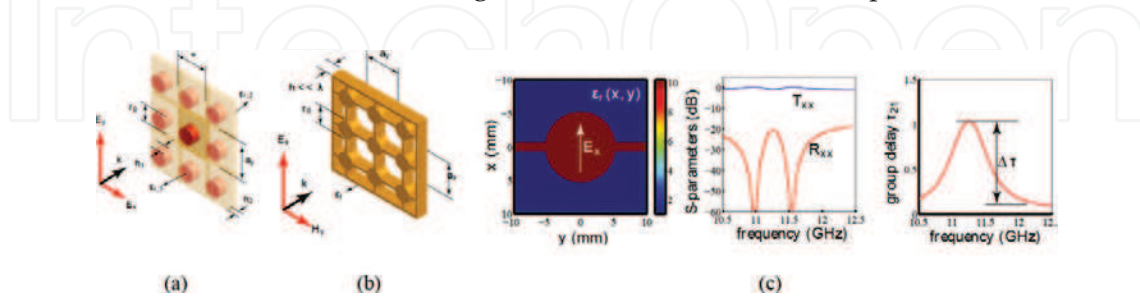

Figure 7. All-dielectric metasurfaces. (a) Conventional all-pass dielectric metasurface and (b) proposed all-pass and all-dielectric metasurface based on 2D array of inter-connected coupled disks [37]. (c) Typical transmission and reflection characteristics of the proposed all-dielectric metasurface with horizontal interconnections. ε_r = 10.2, h = 5.08 mm and interconnection thickness = 2.54 mm [37]. ©IEEE; reprinted with permission.

3.3.2. Proposed phaser based on all-dielectric metasurface

Taking inspiration from the coupled-dielectric metasurfaces of **Figure 7(a)**, **Figure 7(b)** shows an all-dielectric metasurface structure, particularly suitable for microwave and mm-wave frequencies. It consists of a periodic 2D array of dielectric resonators, however, instead of being supported by a host substrate of different permittivity, the resonators are connected to each other via thin dielectric interconnections. The overall structure may be seen as a perforated dielectric substrate, where dielectric material is removed in undesired areas using standard laser hole drilling processes [37].

The dielectric interconnections therefore provide the required mechanical support to hold the dielectric unit cells together. Since there is no host substrate, the proposed structure does not exhibit spurious Fabry-Perot type resonances, unlike in their optical counterparts, while maintaining its inherent all-pass response.

3.3.3. Results

To compute the transmission and reflection characteristics of the proposed structure, shown in **Figure 7(b)**, we used the rigorous coupled-wave analysis (RCWA) [45]. RCWA is a semi-analytical method usually applied to compute scattering parameters in periodic dielectric structures, where the scattered fields are represented as series of spatial harmonics. In this method, the unit cell is represented by a permittivity function ε_r (x, y) in **Figure 7(c)**, which is periodic in the x- and y-directions to form the full metasurface. The two dielectric interconnections are also shown along the x- and y-directions, respectively. The unit cell is incident with a linearly polarized plane-wave E_x, and the corresponding transmission $T_{xx}(\omega)$ and reflection $R_{xx}(\omega)$ response are then obtained using the RCWA method. To be noted is that the unit cell

size is assumed to be subwavelength (i.e., $a_x = a_y \ll \lambda$) so that only the fundamental spatial harmonic exists in the structure.

Figure 7(c) shows the typical transmission and reflection characteristics of the proposed lossless unit cell where only y-oriented interconnections are present. A good matching is achieved with an almost ideally flat transmission response. In addition, a strong dispersion response is observed as desired, as it can be seen from the nonzero group delay swing • τ.

4. Applications

The phasers described in the previous section represent the fundamental units for performing real-time signal processing operations on broadband signals. In this section, two applications are presented in the area of instrumentation and wireless communication, to illustrate the versatility of these phasers.

4.1. Antenna beam scanning in 2D

A common technique to achieve ultrafast signal processing of broadband signals in microwaves and optics is real-time spectrum analysis based on frequency-to-space mapping. While optical diffraction gratings [46] and virtual image phased arrays [47] have been extensively used in optics for spectral decomposition of an optical signal in space, leaky-wave antennas (LWAs) have been used for the same purpose at microwaves with a simpler test signal injection mechanism [18].

Most of these systems are restricted to 1-D decomposition and thus suffer from restricted frequency resolution. An optical system combining two orthogonally placed dispersive components to achieve spectral decomposition in two dimensions of space has recently been proposed [48]. However, the first microwave implementation of a 2D spatial disperser to achieve high-resolution spectrum analysis of broadband microwave signals was presented in Ref. [19].

4.1.1. Spectral decomposition principle

The general objective of a 2D spectral decomposition system is illustrated in **Figure 8(a)**. The temporal frequencies (f_m) of an input signal to analyze ($v_{in}(t)$) are mapped, in real-time, onto different spatial frequencies ($\mathbf{k}_m = (\varphi_m, \theta_m)$) over a two-dimensional plane in space.

A conventional 1D LWA separates the test signal into its frequency components in space following the beam-scanning law of the antenna, where each frequency component is radiated along a specific direction of space according to $\theta_{MB}(\omega) = \sin^{-1}[\beta(\omega)/c]$ [49]. The dispersion relation $\beta(\omega)$ of the radiating structure dictates the mapping between temporal and spatial frequencies, and thus a 1D leaky-wave antenna acts as an analog real-time spectrum analyzer along one dimension of space [18].

To order to extend the functioning of spatial-spectral decomposition from 1D to 2D, in order to increase the frequency resolution in spectrum analysis, we proposed the technique shown in

Figure 8(b). Consider an array of M LWAs excited by phasers [12], as shown in **Figure 8(a)**. Let us assume that each of the LWAs is a composite right/left-handed (CRLH) antenna, covering the signal bandwidth [ω_{start}, ω_{stop}] [49]. Such antennas naturally provide spectral decomposition along the y-axis from forward to backward region including broadside, according to $\beta(\omega) = \omega/\omega_R \bullet \omega_L/\omega$ [18, 49].

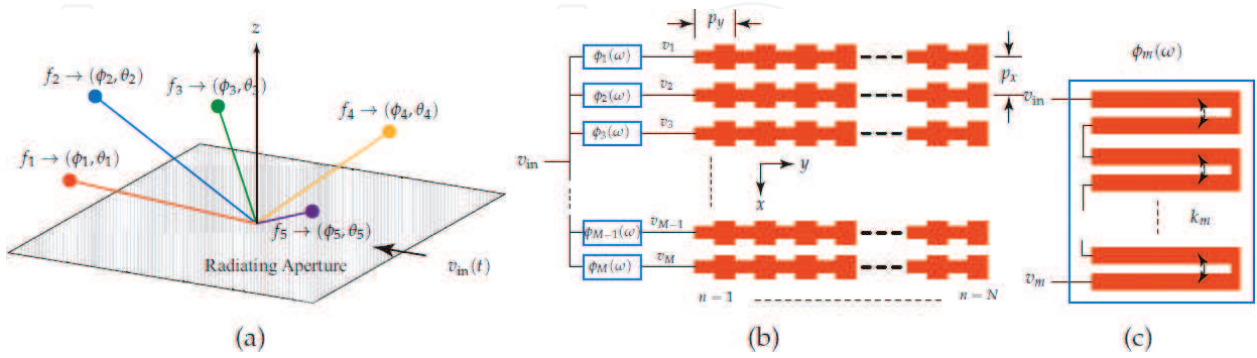(a)   (b)   (c)

Figure 8. Proposed structure for 2D spectral decomposition, consisting of an array of LWAs fed by phasers [19]. (a) Antenna array layout and (b) one of the phasers, which is here a cascaded C-section phaser. ©IEEE; reprinted with permission.

The frequency discrimination along the x-axis is achieved using a dispersive feeding network wherein the mth antenna in the array is connected with a phaser, providing a phase shift $\varphi_m(\omega)$. First assume, for simplicity, that the LWAs only radiate along broadside ($\theta = 0°$) in the $\varphi = 90°$ plane. Consider the radiation at a certain frequency $\omega 0$ in the $\varphi = 0°$ plane for the following three cases:

1. The LWAs are excited in phase, i.e., $|\varphi_{m+1}(\omega_0) \bullet \varphi_m(\omega_0)| = 2k\pi$, where k is an integer: In this case, frequency $\omega 0$ points to broadside, i.e., $\theta = 0°$.

2. $\varphi_{m+1}(\omega_0) \bullet \varphi_m(\omega_0) > 0$: In this case, $\omega 0$ points in the forward direction, i.e., $90° > \theta_{MB} > 0$.

3. $\varphi_{m+1}(\omega_0) \bullet \varphi_m(\omega_0) < 0$: In this situation, the frequency $\omega 0$ radiates in the backward direction, i.e., $\bullet 90° < \theta_{MB} < 0$.

Therefore, an appropriate feeding phasers allows for a full-space frequency scanning along the x-axis. Moreover, if the above three phase conditions are satisfied at several frequency points within the given bandwidth, the backward to forward frequency scan will repeat periodically for each frequency subband. Finally, integrating the x-axis scanning with the conventional y-axis scanning of the antenna results in 2D frequency scanning in space.

4.1.2. Results

Let us assume the cascaded C-section phaser as the dispersive feed element to the array, as shown in **Figure 8(c)**. This phaser consists of several C-sections, which are formed using a coupled-line coupler with a coupling coefficient k. The corresponding transmission phase is given by $\varphi_i(\omega) = \bullet 2q_0\tan^{\bullet 1}(1+k_i)/(1 \bullet k_i)\tan((\pi\omega)/(2\omega_\lambda))$, where q_0 is the number of C-sections in the phaser and ω_λ is the quarter-wavelength frequency of the coupler. The radiation properties

of the overall LWA array of **Figure 8(b)** can then be determined based on the above dispersive network and CRLH LWA dispersion relation.

Figure 9 shows the computed array factor results of several different dispersion characteristics of the feeding section. First, a nondispersive network is assumed (with $k = 0$), as shown in the first row of **Figure 9**. In this case, the LWA array shows conventional 1D scanning along the y-axis, since all the antennas are fed in-phase. Next, a small dispersion in $\varphi(\omega)$ is introduced using $k \neq 0$, as shown in the second row of **Figure 9**. As a result, the frequency scanning plane is rotated to about $\varphi = 45°$ plane. In this case, the frequency point ω_A where $|\varphi_{m+1}(\omega_A) \bullet \varphi_m(\omega_A)| = 0$,

$$AF(\theta, \phi, \omega) = \sum_{n=1}^{N} e^{-j(n-1)k_0 p_y [\sin\theta \sin\phi - \beta(\omega)]} \sum_{m=1}^{M} e^{-j(m-1)k_0 p_x (\sin\theta \cos\phi)} e^{-j\phi_m(\omega)}$$
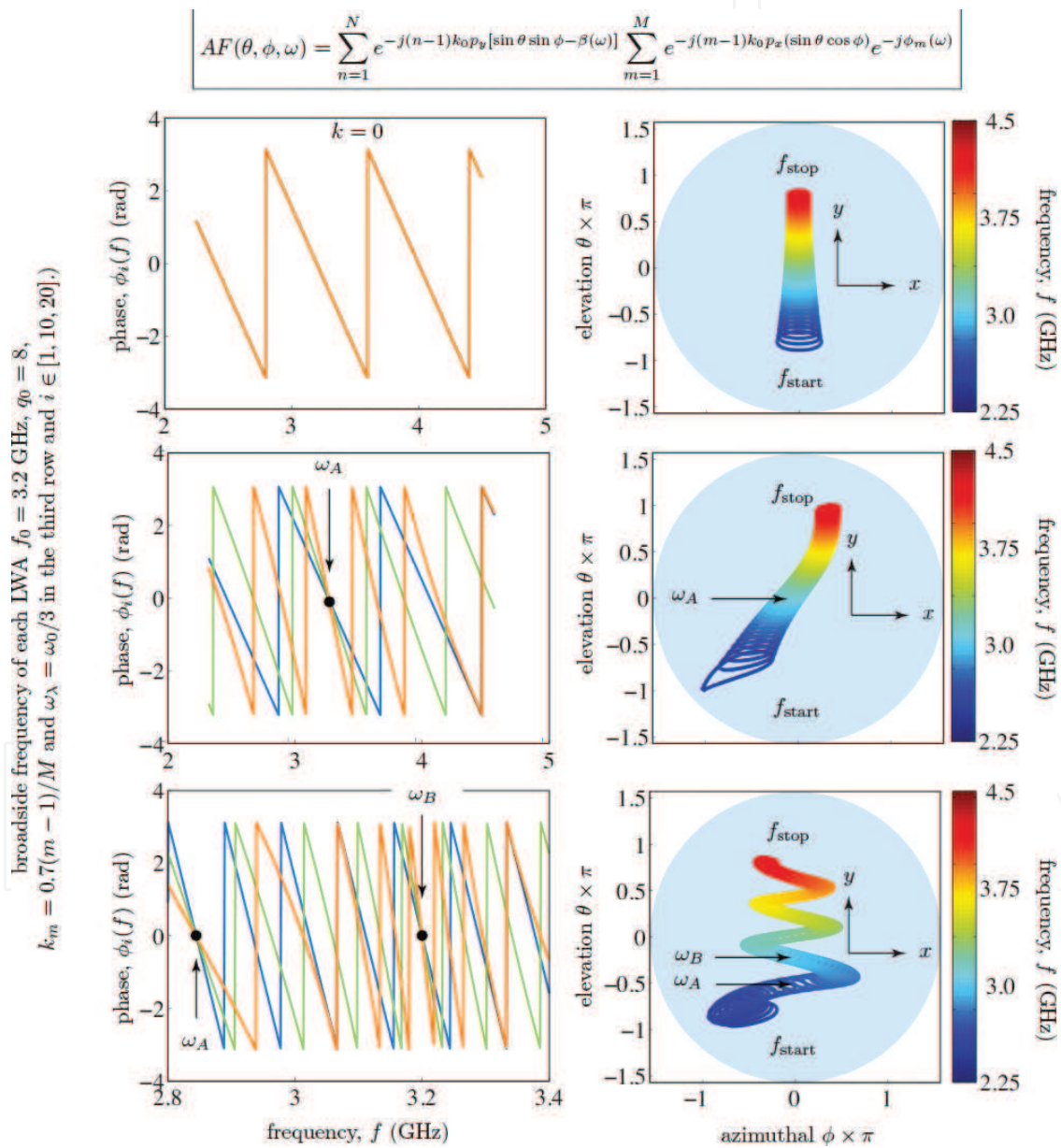

Figure 9. Array factor computed results corresponding to the structure in **Figure 8** with $M \bullet N = 20 \bullet 30$ showing the dispersion profile of the phaser feeding elements at the input of each leaky-wave antenna and the 3-dB contour plots of the 2D radiation patterns in the (θ, φ) plane [19]. ©IEEE; reprinted with permission.

corresponds to the broadside frequency in the $\varphi = 0°$ plane. The interesting case is when the dispersion characteristics of the phaser is periodic in frequency due to its commensurate nature, within the radiating band of the LWA, as shown in the third row of **Figure 9**. In this case, a periodic frequency scanning is achieved between the left and right half of the ($\theta \cdot \varphi$) plane, thereby distributing the same frequency band in a larger area in space leading to a higher frequency resolution.

4.2. Dispersion code multiple access (DCMA) system

The second application of R-ASP presented here is in wireless communication applications. One important concept in wireless communication is *multiple access*. A multiple access technology plays a crucial role in sharing common resources between multiple users in dense wireless communication environments. Typical techniques include frequency domain multiplexing (FDM), time-domain multiplexing (TDM), code division multiple access (CDMA), and space division multiple access (SDMA) [50].

All these techniques are dominantly based on digital technologies, and thus suffer from poor performances at high frequencies and in broadband regimes. Considering their limitations in meeting the future throughput and reliability demands for the next-generation wireless networks, a dispersion code multiple access (DCMA) scheme has been recently introduced in Ref. [51]. Due to its analog and real-time operation, DCMA is naturally scalable to high-frequencies and can accommodate ultra-wideband signals, using efficient phasers [12, 46]. The first rigorous investigation on the bit-error-rate (BER) performance of a DCMA system was recently presented in Ref. [21].

4.2.1. Principle

Consider a three user communication system, as shown in **Figure 10(a)**, where sender A wishes to communicate with receiver B only. Each user is associated with a phaser with a specific group delay versus frequency profile [12]. A linear group delay profile is chosen here for simplicity. Sender A first prechirps and expands a broadband input pulse using a positively sloped delay phaser. It then transmits it to both receivers B and C. While the intended receiver is B, it is able to recompress the pulse using a negatively sloped delay phaser. However, receiver C is unable to retrieve the original signal since the received signal is further expanded due to its positively sloped delay phaser. Therefore, A and B form a secure wireless channel between them, owing to their complementary phaser profiles, since $\tau_A(\omega) + \tau_B(\omega) = \text{const.}, \forall \omega$. In situations where there are more users, each user pair with two complementary phasers forms a wireless channel. Therefore, exploiting several dispersion code pairs, multiple channels can exist in the same frequency band, thereby sharing the available communication resources at the same time. This is the basic concept of DCMA.

4.2.2. Signal propagation modeling

Consider the $N \cdot N$ DCMA system shown in **Figure 10(b)**. The transfer function of the kth transmitting phaser is assumed to have the all-pass from $H_k^{Tx}(\omega) = \exp(j\varphi_k^{Tx})$, with
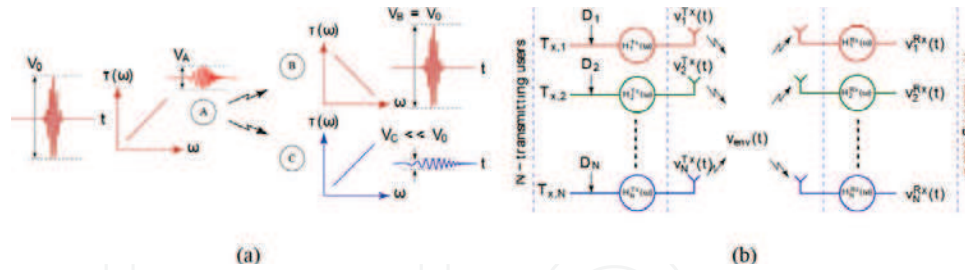
Figure 10. Dispersion code multiple access (DCMA) [21]. (a) Principle. (b) $N \cdot N$ DCMA system. For each transmitter, the intended receiver is indicated with the same color code [21]. ©IEEE; reprinted with permission.

$$\varphi_k^{Tx}(\omega) = -\int_{\omega 1}^{\omega 2} \tau_k^{Tx}(\omega)d\omega = -\varphi_0 - \int_{\omega 1}^{\omega 2} \tau_k^{Tx}(\omega)d\omega, \text{ where } \tau_k(\omega) \text{ is the group delay versus frequency}$$

profile of the phaser, $\varphi_0 = -\tau_0(\omega_2 - \omega_1)$, with τ_0 being the average group delay of the phaser. Similarly, the transfer function of the lth receiving phaser is $H_k^{Rx}(\omega) = \exp(j\varphi_l^{Rx})$, where

$$\varphi_l^{Rx}(\omega) = -\int_{\omega 1}^{\omega 2} \tau_l^{Rx}(\omega)d\omega = -\varphi_0 + \int_{\omega 1}^{\omega 2} \tau_l^{Rx}(\omega)d\omega. \text{ In this example, the } k\text{th transmitting and the } k\text{th}$$

receiving phaser are dispersion matched with complimentary delay responses and thus form the kth wireless channel.

The digital information of user k can be specified by a vector D_k. This information is impressed on a periodically pulsed signal, following an on-off-keying (OOK) modulation format. Following this, the input to the kth transmitting phaser is given by $v_k^{in}(t) = \sum_{m=1}^M D_k(m)a_0(t - mT_0)\sin(\omega_0 t)$, where $a_0(t)$ is a baseband pulse, T_0 is the bit-period and ω_0 is the carrier frequency. The output signal from the kth transmitting phaser is $v_k^{Tx}(t) = F^{-1}[F\{v_k^{in}(t)\}H_k^{Tx}(\omega)]$, where F represents the Fourier transform. When all the users are transmitting together, the total signal in the environment is the sum of all the signals present, and thus is given by $v_{env(t)} = \sum N v_k^{Tx}(t)$. This signal is then received at the lth receiver as $v_l^{Rx}(t) = F^{-1}[F\{v_{env}(t)\}H_{env}(\omega)H_l^{Rx}(\omega)]$, where $H_{env}(\omega)$ is the transfer function of the wireless environment.

The received signal is then demodulated to extract the information using a simple thresholding mechanism. Finally, it is compared with the information D_k, which was originally sent, with $l = k$ at the intended transmitter to determine the bit-error rate in each wireless channel.

4.2.3. Results

An appropriate selection of phaser code profiles, $\tau_k(\omega)$, is important to achieve optimal channel discrimination between the different wireless channels in the DCMA system of **Figure 10**. One attractive choice is based on a set of Chebyshev polynomials, exhibiting a fixed min-max amplitude range in a given region, ensuring that the dispersed pulses are always contained within one-bit period [51]. The corresponding delay response of the kth transmitting phaser can be written $\tau_k(\omega) = \Delta\tau[\tau_k(\omega)] + \tau_0$, with $\omega = 2(\omega - \omega_0)/(\omega_2 - \omega_1)$, where $\tau_k(\omega)$ is the kth Chebyshev polynomial of the first kind, $\Delta\tau$ is the delay swing, and $(\omega_2 - \omega_1)$ is the bandwidth of $a_0(t)$. Some typical Chebyshev delay codes are plotted in **Figure 11(a)** along with their complementary responses.

Next, to estimate the bit-error rate (BER) of an *ideal DCMA system*, these assumptions were made: (1) direct line-of-sight transmission with no multiple reflections, (2) nondispersive channels, i.e., $H_{\mathrm{env}}(\omega)$ = const. = 1, and (3) noiseless environment. **Figure 11(b)** shows the numerically computed BERs for different Chebyshev codes and delay swing • τ's. A 20-bit data stream is specified at each transmitting location, and the corresponding BER is computed as an average of multiple simulation data. When only odd Chebyshev polynomials are used (third column), the BER of all channels progressively drops to zero as • τ is increased. This simulation suggests that odd Chebyshev codes are excellent candidates for DCMA.
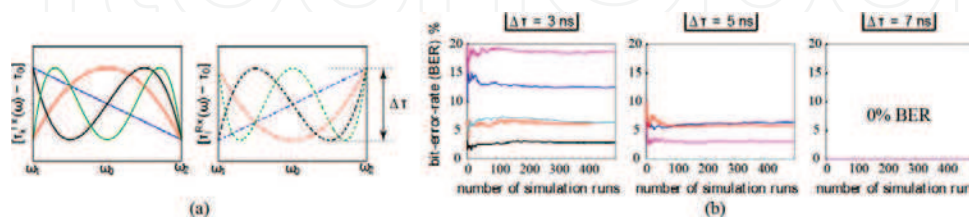

Figure 11. DCMA system results [21]. (a) Typical Chebyshev delay codes and (b) the computed BERs for a 5 • 5 DCMA system with different odd-order only Chebyshev delay profiles and delay swings • τ's for the following parameters: T_0 = 20 ns, $a_0(t)$ is Gaussian pulse with full-width half maximum (FWHM) of 0.25 ns, $\omega_0 = (\omega_2 \bullet \omega_1) = 2\pi$ (5 GHz). Each color corresponds to a wireless channel between two intended transmitters and receivers. ©IEEE; reprinted with permission.

While the DCMA technology is presented here for multiple-access, it is ideally suited for enhancing the data throughput of a single wireless channel. Consider the DCMA system of **Figure 10(b)**, and assume that the serial data stream of a signal transmitter is converted into N parallel streams, which are then modulated through unique phaser dispersions across each of the N channels. Using the DCMA principle described above, each of these parallel data streams can be retrieved on the receiver side of the system, and combined back to produce the final output data stream. By increasing N, larger amount of data can be simultaneously transmitted within the same bandwidth. Such a system has been recently described as a dispersion code modulation (DCM) system [22].

5. Conclusions

In the context of the exploding demands for future wireless networks, R-ASP has been presented as a novel signal processing paradigm. Due to its analog and real-time nature, it represents a fundamentally different technology to manipulate and control radio signals, in contrast to conventional DSP techniques, particularly suited for microwave and mm-wave systems. In this chapter, recent developments in R-ASP technology have been presented in detail. Several novel passive and active phasers, based on coupled-line couplers have been discussed along with their spatial counterparts using all-dielectric metasurface structures. Finally, two applications have been presented: a 2D real-time spectrum analyzer and a DCMA system, to illustrate the applicability of such phasers in instrumentation and communication systems, respectively.

Author details

Shulabh Gupta[1]* and Christophe Caloz[2]

*Address all correspondence to: shulabh.gupta@carleton.ca

1 Department of Electronics, Carleton University, Ottawa, Ontario, Canada

2 Department of Electrical Engineering, Polytechnique Montréal, Montréal, Québec, Canada

References

[1] Huawei, "5g: A technology vision," White Paper, 2013.

[2] Ericsson, "The real-time cloud," White Paper, 2013.

[3] A. Osseiran, "The foundation of the mobile and wireless communications systems for 2020 and beyond: Challenges, enablers and technology solutions", Proc. IEEE 77th Veh. Tech. Conf., 2013-June.

[4] F. Boccardia, B. L. Alcatel-Lucent, R. W. H. J. T. U. of Texas at Austin, A. L. U. P. Fabra, A. L. Thomas L. Marzetta (Bell Labs, and P. A. University), "Five disruptive technology directions for 5g."

[5] W. Chin, Z. Fan, and T. R. Haines, "Emerging technologies and research challenges for 5g wireless networks," Toshiba Research Europe Limited, Bristol, UK.

[6] S. Gupta, "Automatic analog beamforming transceiver for 60 ghz radios," University of California, Los Angeles.

[7] "Defining the future of multi-gigabit wireless communications," WiGig white paper, 2010.

[8] "The 60 ghz band cuts 4g backhaul costs," Electronic Design Article, 2013.

[9] D. Halperin, S. Kandula, J. Padhye, and D. Wetherall, "Augmenting data center networks with multi-gigabit wireless links," Microsoft Research and University of Washington, 2011.

[10] N. Hamedazimi, H. Gupta, V. Sekar, and S. R. Das, "Patch panels in the sky: A case for free-space optics in data centers," Department of Computer Science, Stony Brook University, Stony Brook, NY, USA.

[11] "Millimeter waves: Emerging markets brochure," A Thintri Market Study, 2012.

[12] C. Caloz, S. Gupta, Q. Zhang, and B. Nikfal, "Analog signal processing: a possible alternative or complement to dominantly digital radio schemes," IEEE Microw. Mag., vol. 14, no. 6, pp. 87–103, Sep. 2013.

[13] J. D. Schwartz, I. Arnedo, M. A. G. Laso, T. Lopetegi, J. Azaña, and D. Plant, "An electronic UWB continuously tunable time-delay system with nanosecond delays," IEEE Microw. Wireless Compon. Lett., vol. 18, no. 2, pp. 103–105, Jan. 2008.

[14] B. Nikfal, S. Gupta, and C. Caloz, "Increased group delay slope loop system for enhanced-resolution analog signal processing," IEEE Trans. Microw. Theory Tech., vol. 59, no. 6, pp. 1622–1628, Jun. 2011.

[15] B. Nikfal, D. Badiere, M. Repeta, B. Deforge, S. Gupta, and C. Caloz, "Distortion-less real-time spectrum sniffing based on a stepped group-delay phaser," IEEE Microw. Wireless Compon. Lett., vol. 22, no. 11, pp. 601–603, Oct. 2012.

[16] S. Abielmona, S. Gupta, and C. Caloz, "Compressive receiver using a CRLH-based dispersive delay line for analog signal processing," IEEE Trans. Microw. Theory Tech., vol. 57, no. 11, pp. 2617–2626, Nov. 2009.

[17] S. Gupta, B. Nikfal, and C. Caloz, "Chipless RFID system based on group delay engineered dispersive delay structures," IEEE Antennas Wirel. Propagat. Lett., vol. 10, pp. 1366–1368, Dec. 2011.

[18] S. Gupta, S. Abielmona, and C. Caloz, "Microwave analog real-time spectrum analyzer (RTSA) based on the spatial-spectral decomposition property of leaky-wave structures," IEEE Trans. Microw. Theory Tech., vol. 59, no. 12, pp. 2989–2999, Dec. 2009.

[19] S. Gupta and C. Caloz, "Real-time 2-d spectral-decomposition using a leaky-wave antenna array with dispersive feeding network," in 2015 IEEE International Symposium on Antennas and Propagation USNC/URSI National Radio Science Meeting, July 2015, pp. 29–30.

[20] H. V. Nguyen and C. Caloz, "Composite right/left-handed delay line pulse position modulation transmitter," IEEE Microw. Wireless Compon. Lett., vol. 18, no. 5, pp. 527–529, Aug. 2008.

[21] S. Gupta, L. Zou, M. A. Salem, and C. Caloz, "Bit-error-rate (ber) performance in dispersion code multiple access (dcma)," in 2015 IEEE International Symposium on Antennas and Propagation USNC/URSI National Radio Science Meeting, July 2015, pp. 1015–1016.

[22] L. Zou, S. Gupta, and C. Caloz, "Dispersion code modulation concept for spectral efficiency enhancement in wireless communications," in IEEE International Symposium on Antennas and Propagation, Jun. 2016.

[23] B. Nikfal, Q. Zhang, and C. Caloz, "Enhanced-snr impulse radio transceiver based on phasers," IEEE Microwave and Wireless Components Letters, vol. 24, no. 11, pp. 778–780, Nov. 2014.

[24] B. Nikfal and C. Caloz, "Low-complexity and frequency-scalable analog real-time fdm receiver based on a dispersive delay structure," in Microwave Conference (EuMC), 2011 41st European, Oct 2011, pp. 397–400.

[25] M. A. G. Laso, T. Lopetegi, M. J. Erro, D. Benito, M. J. Garde, M. A. Muriel, M. Sorolla, and M. Guglielmi, "Chirped delay lines in microstrip technology," IEEE Microw. Wireless Compon. Lett., vol. 11, no. 12, pp. 486–488, Dec. 2001.

[26] Q. Zhang, S. Gupta, and C. Caloz, "Synthesis of narrow-band reflection-type phaser with arbitrary prescribed group delay," IEEE Trans. Microw. Theory Tech., vol. 60, no. 8, pp. 2394–2402, Aug. 2012.

[27] C. K. Campbell, Surface Acoustic Wave Devices and Their Signal Processing Applications. San Diego, USA: Academic Press, 1989.

[28] W. S. Ishak, "Magnetostatic wave technology: a review," Proc. IEEE, vol. 76, no. 2, pp. 171–187, Feb. 1988.

[29] Q. Zhang, D. L. Sounas, and C. Caloz, "Synthesis of cross-coupled reduced-order phasers with arbitrary group delay and controlled magnitude," IEEE Trans. Microw. Theory Tech., vol. 61, no. 3, pp. 1043–1052, Mar. 2013.

[30] H.-T. Hsu, H.-W. Yao, K. A. Zaki, and A. E. Atia, "Synthesis of coupled-resonators group-delay equalizers," IEEE Trans. Microw. Theory Tech., vol. 50, no. 8, pp. 1960–1968, Aug. 2002.

[31] E. G. Cristal, "Theory and design of transmission line all-pass equalizers," IEEE Trans. Microw. Theory Tech., vol. 17, no. 1, pp. 28–38, Jan. 1969.

[32] S. Gupta, A. Parsa, E. Perret, R. V. Snyder, R. J. Wenzel, and C. Caloz, "Group delay engineered non-commensurate transmission line all-pass network for analog signal processing," IEEE Trans. Microw. Theory Tech., vol. 58, no. 9, pp. 2392–2407, Sept. 2010.

[33] Q. Zhang, S. Gupta, and C. Caloz, "Synthesis of broadband phasers formed by commensurate C- and D-sections," Int. J. RF Microw. Comput. Aided Eng., Aug. 2013.

[34] S. Gupta, Q. Zhang, L. Zou, L. J. Jiang, and C. Caloz, "Generalized coupled-line all-pass phasers," IEEE Trans. Microw. Theory and Tech., vol. 63, no. 3, pp. 1007–1018, March 2015.

[35] L. Zou, S. Gupta, and C. Caloz, "Reconfigurable phaser using gain-loss c-sections for radio analog signal processing (r-asp)," in 2015 Asia-Pacific Microwave Conference (APMC), vol. 3, pp. 1–3, Dec. 2015.

[36] L. F. Zou, S. Gupta, and C. Caloz, "Loss-gain equalized reconfigurable C-section analog signal processor," in IEEE Transactions on Microwave Theory and Techniques, vol. PP, no. 99, pp. 1–10, Oct. 2016, in press. doi: 10.1109/TMTT.2016.2615920.

[37] S. Gupta, K. Achouri, and C. Caloz, "All-pass metasurfaces based on interconnected dielectric resonators as a spatial phaser for real-time analog signal processing," in 2015 IEEE Conference on Antenna Measurements Applications (CAMA), pp. 1–3, Nov. 2015.

[38] N. Yu and F. Capasso, "Flat optics with designer metasurfaces," Nat. Mater., vol. 13, pp. 139–150, April 2014.

[39] K. Achouri, M. A. Salem, and C. Caloz, "General metasurface synthesis based on susceptibility tensors," IEEE Trans. Antennas Propag., vol. 63, no. 7, pp. 2977–2991, Jul 2015.

[40] C. Pfeiffer and A. Grbic, "Controlling vector bessel beams with metasurfaces," Phys. Rev. Appl., vol. 2, p. 044012, Oct. 2014.

[41] A. Shaltout, A. Kildishev, and V. Shalaev, "Time-varying metasurfaces and lorentz nonreciprocity," Opt. Mater. Express, vol. 5, no. 11, pp. 2459–2467, Nov. 2015.

[42] Y. Hadad, D. L. Sounas, and A. Alu, "Space-time gradient metasurfaces," Phys. Rev. B, vol. 92, p. 100304, Sep. 2015.

[43] M. Decker, I. Staude, M. Falkner, J. Dominguez, D. N. Neshev, I. Brener, T. Pertsch, and Y. S. Kivshar, "High-efficiency light-wave control with all-dielectric optical huygens' metasurfaces," pp. 813–820, May 2014.

[44] A. Arbabi, Y. Horie, M. Bagheri, and A. Faraon, "Complete control of polarization and phase of light with high efficiency and sub-wavelength spatial resolution," arXiv:1411.1494, pp. 4308–4315, Nov. 2014.

[45] M. G. Moharam and T. K. Gaylord, "Rigorous coupled-wave analysis of planar-grating diffraction," J. Opt. Soc. Am., vol. 71, no. 7, pp. 811–818, Jul 1981.

[46] J. Goodman, Introduction to Fourier Optics. Englewood, CO: Roberts and Company Publishers; 3rd edition, 2004.

[47] M. Shirasaki, "Large angular dispersion by a virtually imaged phased array and its application to a wavelength demultiplexer," Opt. Lett., vol. 21, no. 5, pp. 366–368, Mar. 1996.

[48] C. Dragone and J. Ford, "Free-space/arrayed-waveguide router," US Patent 6,263,127, 2001.

[49] C. Caloz, D. R. Jackson, and T. Itoh, "Leaky-wave antennas (chap. 9)," in Frontiers in Antennas: Next Generation Design and Engineering, F. B. Gross, Ed. McGraw Hill, 2011.

[50] J. G. Proakis and M. Salehi, Digital Communications, 5th ed. McGraw-Hill Science/Engineering/Math, 2007.

[51] B. Nikfal, M. Salem, and C. Caloz, "A method and apparatus for encoding data using instantaneous frequency dispersion," US 62/ 002,978, Nov. 2013.